RSC Advances

ROYAL SOCIETY OF CHEMISTRY

www.rsc.org/advances

CREATED USING THE RSC LaTeX PCCP ARTICLE TEMPLATE – SEE www.rsc.org/electronicfiles FOR DETAILS

ARTICLE TYPE www. rsc.org/xxxxxx | XXXXXXXX

Effects of Non-catalytic Surface Reactions on the CH_4/Air Premixed Flame within Micro-channels

Zhenhua Xie,[ab] Zhongqing Yang,[ab] Li Zhang,*[ab] and Chuncheng Liu[a]

Received Xth XXXXXXXXXX 20XX, Accepted Xth XXXXXXXXX 20XX

First published on the web Xth XXXXXXXXXX 200X

DOI: 10.1039/b000000x

The non-catalytic surface of the micro-combustor plays a significant role in flame propagation. For the purpose of investigating the effects of surface reactions on combustion process, this paper presents a numerical 2D simulation of a CH_4/air premixed flame within a micro planar channel with detailed gas-phase and non-catalytic surface reaction mechanisms. In this paper, we focus on numerically examining the effects of surface reactions on flame structure. The simulation results show that surface reactions affect the temperature distribution in three controlling regimes distinguished according to the inlet velocity. Besides, radicals suffer sharper declines near the active surface than those near the inert surface due to the radical removing effect. Moreover, as the temperature increases, the difference will become more remarkable especially in the vicinity of the wall. Among the radicals, the mass fraction of H, O, and OH & CH_3 near the surface experiences the largest, mediate and the smallest decay, respectively, when changing the inert surface to the active surface. The adsorption of H should be of the greatest concern. OH radical has the similar distribution profiles as O radical for both kinds of surfaces.

1 Introduction

With the advances in the fabrication technologies for micro-electromechanical systems (MEMS), the micro-burners of millimeter scale have been widely developed and applied for various micro-thrusters[1–3], micro-engines[4–6] and micro-reactor[7–10] in the past decades. These applications were mainly due to the fact that hydrocarbon fuels based micro-burners shows a higher energy density, compared with the most advanced currently available lithium ion batteries.[11] However, with the decrease of the combustor size, the combustor surface to volume ratio increases dramatically, creating strong flame-wall interaction and the flame could be quenched.[12] The quenching mechanisms mainly consist of thermal and kinetic mechanisms, i.e., heat loss to wall and radical adsorption on the surface.[13–15] Thus, the surface of the micro-combustor plays a significant role in flame propagation.

In the past decades, many efforts have been made on the kinetic mechanism especially with the catalytically active surfaces.[16–22] However, the kinetic mechanism on non-catalytic surfaces (such as quartz and chromium surfaces) did not draw much attention and their effects within micro-burners are not well understood. Vlachos et al. investigated the radical quenching mechanism, i.e., kinetic mechanism, in ignition and extinction of flames for premixed hydrogen/air near surfaces with detailed gas-phase mechanism and they treated the wall as a sink of radicals.[23,24] Raimondeau et al. conducted 2D simulations of flame propagation of methane/air and the gas-phase interaction, using detailed gas-phase mechanism and radical quenching mechanism.[15] They showed that the flames could propagate within micro-channels by preheating and insulation, and the near-entrance heat loss and radical quenching at the wall are the two key issues for flame propagation in micro-channels. Aghalayam et al. investigated the role of radical quenching in flame stability of hydrogen-air mixtures and wall heat flux.[25] They claimed that the ignition is retarded solely by the kinetics of surface reactions, while the extinction is controlled by both the kinetics and thermal feedback from radical recombination on the wall. The combustion of methane was studied by Rahmat Sotudeh-Gharebagh et al. in a fixed bed reactor to determine the effect of inert particles at distinct temperature intervals.[26] They found that sand particles might act as catalysts to increase conversion at low temperature ($\sim$ 750 °C) but with quite small contribution. Besides, wall surfaces inhibited homogeneous combustion by reducing free radical concentrations at moderately high temperatures ($750-850$ °C), and the inhibition effects became less significant and could be neglected compared with rapid homogeneous reactions at high temperatures (above $875-900$ °C). Miesse et al. experimentally studied the effects of wall temperature and materials on radical quenching.[27] They found that the thermal quenching dominates at a colder surface (near 500 K) since the quenching lengths were relatively independent of wall materials, whilst

[a] *Key Laboratory of Low-grade Energy Utilization Technology and Systems (Chongqing University), Ministry of Education of PRC, Chongqing 400044, China.*

[b] *College of Power Engineering, Chongqing University, Chongqing 400044, PR China. Fax: +86 (023) 651 11832; Tel: +86 (023) 651 03114; E-mail: lizhang_cqu@163.com*

the quenching lengths strongly depend on wall material at higher temperatures (near 1273 K) with radical quenching controlling the process. Kim et al. experimentally examined the significance of the two quenching mechanisms.[14] Three distinct controlling regimes occurred during quenching behaviors, representing thermal regime ($100-350$ °C), heterogeneous reaction regime ($400-600$ °C), and gas-phase reaction regime (above 600 °C), respectively. Saiki et al. combined OH-PLIF/micro-OH-PLIF and numerical simulation to estimate the initial sticking coefficients associated with radical adsorption, and the results confirmed there should exist radical quenching effect for quartz surface.[28] Bai et al. proposed an analytic model to provide an access to theoretically analyze flame propagation with both thermal and radical quenching mechanisms, using a model with two gaseous chain-branching reactions and one step surface reaction.[13] Even though previous studies have experimentally and numerically investigated the dependence of quenching distances on materials, there are quite few researches conducted to directly reflect the kinetic effects especially with detailed gas-phase and surface reaction mechanisms. Thus we still do not have a deeper insight into the effects of radical quenching on combustion characteristics. Fortunately, simulation might give access to fundamentally understanding the radical quenching effects.

Obviously, the surface reactions initially affect the radical distribution especially near the wall, further impact the reaction rates and heat release, and subsequently influence the temperature profiles. In this work, the emphasis is imposed on numerically examining the effects of non-catalytic wall surface reactions, i.e., radical-removing effects, on flame structure, since it is significant to characterize the combustion process. In case of misunderstanding, the surfaces discussed hereafter are non-catalytic surfaces instead of traditionally catalytic ones. In this paper, the "active surface" and "inert surface" refer to the non-catalytic (radical-removing) surface and the completely inert surface, respectively.

2 Model Description

2.1 Physical Model

The 2D cross-sectional view (5×1 mm^2) of reactor is shown in Figure 1. The micro-burner consists of two parallel, infinitely wide plates. The combustion within micro-burners is normally accompanied with complex radical and thermal effects, making that these reactors are quite different from classic CSTR (Continuous Stirred Tank Reactor) and PFR (Plug Flow Reactor). In this paper, our primary focus is on understanding the effects of wall surface reactions within the micro-reactor, instead of the thermal effects. Thus, the thickness of wall is set as zero, so as to remove the wall heat conduction effects. Besides, the plates are set as isothermal and thereby heat recirculation is not necessarily considered in the present model. Since the premixed, preheated CH_4/air mixture enters into the gap of two parallel plates, meaning a symmetrical flow with respect to the centerline, only half of the reactor is taken as the computational domain for time saving.

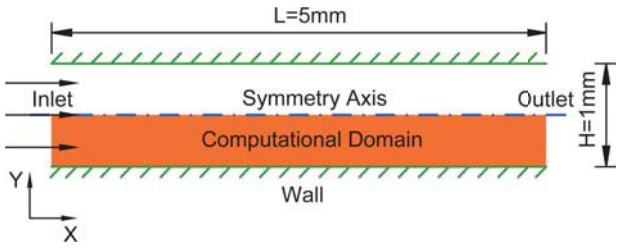

Fig. 1 Schematic diagram of the 2D reactor with 5 mm of length (L) and 1 mm of height (H).

2.2 Numerical Model

Based on the above descriptions and assumptions, the governing conservation equations of mass, momentum, and species as well as ideal gas law are listed as follow:

$$\frac{\partial \rho}{\partial t}+\nabla\cdot(\rho U)=0 \tag{1}$$

where ρ is the fluid density (kg/m^3), t is the time (s), ∇ is the spatial gradient operator, $\cdot$ is the vector dot product, and U is the absolute velocity (m/s).

$$\rho\frac{\mathrm{D}u}{\mathrm{D}t}=-\frac{\partial P}{\partial x}+\frac{\partial}{\partial x}\left(2\mu\frac{\partial u}{\partial x}-\frac{2}{3}\mu\nabla\cdot v\right)+\frac{\partial}{\partial y}\left[\mu\left(\frac{\partial u}{\partial y}+\frac{\partial v}{\partial x}\right)\right] \tag{2}$$

$$\rho\frac{\mathrm{D}v}{\mathrm{D}t}=-\frac{\partial P}{\partial y}+\frac{\partial}{\partial y}\left(2\mu\frac{\partial v}{\partial y}-\frac{2}{3}\mu\nabla\cdot v\right)+\frac{\partial}{\partial x}\left[\mu\left(\frac{\partial u}{\partial y}+\frac{\partial v}{\partial x}\right)\right] \tag{3}$$

where P is the absolute pressure (pa), and μ is the dynamic viscosity (N·s/m^2). x and y indicate the axial and transverse position (mm), respectively. u and v represent the axial and transverse velocity (m/s), respectively.

$$\rho\frac{\partial Y_i}{\partial t}+\rho u\frac{\partial Y_i}{\partial x}+\rho v\frac{\partial Y_i}{\partial y}=\frac{\partial}{\partial x}\left(\rho D_{i,m}\frac{\partial Y_i}{\partial x}\right)+\frac{\partial}{\partial y}\left(\rho D_{i,m}\frac{\partial Y_i}{\partial y}\right)-R_i \tag{4}$$

where Y_i is the mass fraction of ith species, $D_{i,m}$ is the diffusivity of species i (m^2/s), R_i is the production rate of ith species

(kg/m^3/s).

$$c_p\left[\frac{\partial(\rho T)}{\partial t}+\frac{\partial(\rho uT)}{\partial x}+\frac{\partial(\rho vT)}{y}\right]=\frac{\partial}{\partial x}\left(\lambda\frac{\partial T}{\partial x}\right)+\frac{\partial}{\partial y}\left(\lambda\frac{\partial T}{\partial y}\right)-\sum_{i=1}^{N}h_iR_i \quad (5)$$

where c_p is the constant pressure specific heat (J/K/mol), T is the temoerature (K), λ is the thermal conductivity (W/m/K), h_i is the specific enthalpy of species i (J/kg), and N is the number of gas-phase species.

$$P=\rho RT\sum_{i=1}^{N}\frac{\mathrm{Y_i}}{\mathrm{M_i}} \quad (6)$$

where R is the universal gas constant (J/mol/K), and M_i is the molar mass of species i (kg/mol).

The idea used to calculate the rates of the surface reactions is shown by Eqs. (7) - (10)[29]:

$$R_{s,i}=\sum_{k=1}^{K_s}\upsilon_{ik}k_{fk}\prod_{j=1}^{N_g+N_s}[X_j]^{\upsilon_{jk}},(i=1,...,N_g+N_s) \quad (7)$$

$$k_{fk,a}=\left(\frac{S_{0,i}}{1-S_{0,i}/2}\right)\frac{1}{\Gamma^{\tau}}\sqrt{\frac{RT}{2\pi M_i}} \quad (8)$$

$$k_{fk,s}=A_kT^{\beta_k}\exp\left(-\frac{E_k}{RT_s}\right) \quad (9)$$

$$[X_j]=\Gamma\theta_j,(j=1,...,N_s) \quad (10)$$

where υ_{ik} is the stoichiometric coefficient of species i in kth reaction, k_{fk} is the forward rate constant of kth reaction (kg/mol/s), $[X_j]$ is the molar concentration of jth surface species (mol/m^2). N_g and N_s indicate the number of species in the gaseous phase and wall surface, respectively. $S_{0,i}$ is the sticking coefficient of species i. The surface site densities (Γ) of chromium (3.170×10^{-9} mol/cm^2) and γ-Al_2O_3 (1.360×10^{-9} mol/cm^2) are estimated via the distance between the atoms of lattice.[28] The superscript $^{\tau}$ is the number of sites occupied by the reactant species. The subscript $_a$ and $_s$ represent the adsorption and surface reaction, respectively. θ is the surface coverage.

2.3 Reaction Mechanisms

The gas-phase mechanism of CH_4/air includes 50 species and 309 reactions (GRI-mech 3.0[30] excluding Ar, C_3H_8 and C_3H_7 species and associated reactions). The heterogeneous mechanism shown in Table 1 is the same as in Refs. 15 and 28, containing 5 surface species and 10 elementary surface reactions along with corresponding kinetic parameters. Previous work[31] has analyzed the sensitivity of homogeneous ignition and extinction to radical quenching by examining the difference in ignition and extinction temperatures respectively for adsorptive surfaces (where an intermediate species (CH_3O, HCO, OH, O, HO_2, H or CH_3) is selectively removed) from those for inert surfaces (no adsorption). The sensitivity analysis showed that radicals (shown in Table 1) CH_3/H and H/OH/O have a significant effect on the ignition and extinction near the surfaces, respectively. The heterogeneous mechanism takes radicals adsorption, recombination on surface, and stable gas-phase species desorption into account.

It is necessary to discuss the uncertainties of the parameters in Table 1 and the sensitivity of the results to them as follow:

The initial sticking coefficient (S_0) of each radical adsorption on non-catalytic and inert surfaces is set as one (the strongest quenching affinity) and zero (the weakest quenching affinity), respectively.[15,28] S_0 depends on the binding energy of the adsorbate on metals, since higher binding energy leads to easier adsorption to the surface. From the d-band theory, the bond strength of the adsorbate-surface relies on the metal d-band center relative to the Fermi level.[32,33] The d-band center is a function of the filling of the anti-bonding states (d-band) of the adsorbates on transition metals.[32] As we move left in the periodic table, the anti-bonding states will move up in energy and become less filled, resulting in the d-band center moving up relative to the Fermi level, hence the stronger bonding. Thus, it is reasonable to approximately set S_0 as one for chromium, since $S_0=1$ in precious Pt and Pd cases[34] which have more filled anti-bonding states than chromium (generally non-catalytic for methane combustion). The zero sticking coefficient could be related to the γ-Al_2O_3 surface usually treated as the inert surface.[28]

The pre-exponential factor of each radical recombination is set as 10^{13} s^{-1}, roughly calculated via transition theory.[32] When a molecule adsorbs on the surface, it will lose the major part of its gas-phase entropy, since its translational and rotational degrees of freedom typically become constrained.[35] Therefore, the major contribution to adsorbed molecule entropy is the small vibrational component. For adsorbed atoms, the residual entropy from electronic contribution is so small that could be ignored. Given the above, the entropic change for the radicals recombination is quite small and even could be ignored.[35] Therefore, in the absence of large entropic effects, it is reasonable to approximate the pre-exponential factor by k_BT/h, $\sim10^{13}$ s^{-1}. k_B and h are Boltzmann constant and Planck constant, respectively.

We treat the surface recombination non-activated[15,28] based on two reasons. Firstly, even though we can not experimentally measure the activation barrier for each elementary reaction, we can estimate them by the principle of microscopic reversibility[36] and the Brønsted-Evans-Polanyi (BEP) relation[37] between activation energy and dissociative chemisorption energy. Based on many experiments and DFT calculations, Nørskov et al. re-

alized that for dissociative adsorption processes involving simple diatomic molecules, the slope of the BEP equation is often close to 1, implying that the transition state energy is similar to that of the final state.[32] Combining this rule of thumb with the principle of microscopic reversibility[36], one could estimate that the activation barrier of the reversible reaction (surface recombination) of the surface dissociative reaction is close to 0. Secondly, the activation energy do not play an important role in the total rate of surface reaction, since the radical quenching is adsorption-limited. Even though the real activation barrier might be non-zero, even quite large, assuming on the order of 100 kJ/mole, the rate of the surface combination is about 10^8 s^{-1}, still three magnitude larger than that of the adsroption (on the order of 10^5 s^{-1}). Thus, our non-activated assumption makes no or quite small difference to the results.

The most critical value for the results is the initial sticking coefficient. The rates of radical adsorption and surface recombination estimated from equations (7) and (8) are on the order of 10^5 and 10^{13} s^{-1}, respectively. Thus, we can suppose that the rate-determing step for radical quenching is the radical adsorption process. In order to validate that, we also performed a sensitivity analysis in our preliminary calculations by examining how the flame structure changes as the pre-exponential factor varies from 10^8 to 10^{13} s^{-1}. The results showed the flame structure kept unchanged for all the involved pre-exponential factors. Therefore, the most crucial value for radical quenching effects is S_0, completely the same as in Ref. 28.

We expect to use the CHEMKIN thermodynamic and transport database.[38] Unfortunately, to the authors′ knowledge, there is no thermodynamic data of surface species for the common experimental materials (chromium, γ-Al_2O_3, quartz, etc.) except for catalysts (Pt, Pd, etc.). Therefore, isothermal boundary condition is imposed on the wall, so that we do not have to neither obtain the thermodynamic data of surface adsorbed species nor calculate the heat released by the surface reactions.

Table 1 Heterogeneous mechanism and kinetic parameters.[15,28]

No.	Reactions	S_0 or A (s^{-1})	β	E (kJ/mol)
1	$CH_3 + * \Rightarrow CH_3{}^*$	1	-	-
2	$H + * \Rightarrow H^*$	1	-	-
3	$O + * \Rightarrow O^*$	1	-	-
4	$OH + * \Rightarrow OH^*$	1	-	-
5	$2CH_3{}^* \Rightarrow C_2H_6 + 2*$	10^{13}	0	0
6	$CH_3{}^* + H^* \Rightarrow CH_4 + 2*$	10^{13}	0	0
7	$2H^* \Rightarrow H_2 + 2*$	10^{13}	0	0
8	$2OH^* \Rightarrow H_2O + O^* + *$	10^{13}	0	0
9	$2O^* \Rightarrow O_2 + 2*$	10^{13}	0	0
10	$OH^* + H^* \Rightarrow H_2O + 2*$	10^{13}	0	0

* refers to the surface site in which the radicals are adsorbed; * represents the adsorbed surface species; S_0 indicates the initial sticking coefficient or sticking probability; A is the pre-exponential factor (s^{-1}); β shows the temperature exponent; E is the activation energy (kJ/mol).

2.4 Boundary Conditions and Initial Conditions

Inlet: $(Y_i)_{x=0} = Y_{i,in}(\Phi), (T)_{x=0} = T_s, u = u_0, v = 0$
Outlet: $(\frac{\partial \Psi}{\partial x})_{x=L}, (\Psi = u, v, Y_i, T)$
Wall Surface: $u = v = 0, T = T_s, -\rho D_i(\frac{\partial Y_i}{\partial y})_s = M_i \Gamma R_j, (j =$ H, O, OH, CH_3), $(\frac{\partial Y_i}{\partial y})_s = 0, (i \neq j)$
Axis: $(\frac{\partial \Psi}{\partial x})_{y=H/2} = 0, (\Psi = u, Y_i, T), v = 0$
Initialization: $T(x) = 1800K, T_s = T_{in}, Y_i(x) = Y_{i,in}$
where the subscript $_s$ and $_{in}$ represent the wall surface and the combustor inlet, respectively. Φ is the equivalence ratio, and Ψ is the collection of the parameters.

2.5 Adaptability of Model

The governing equations are discretized by a finite-volume method and solved by Fluent Release 6.3.26. Unsteady simulations are conducted unless otherwise stated. A first-order upwind scheme is introduced to discretize the governing equations and SIMPLE algorithm is used to solve the pressure-velocity coupling. To solve the governing equations implicitly, a 2D segregated solution solver is used with an under-relaxation method. The convergence criteria for residuals of governing equations are set to be 1×10^{-5} for continuity, 1×10^{-5} for velocity, 1×10^{-6} for energy and 1×10^{-5} for species concentration. The residuals are monitored throughout the simulation process. The density is calculated using impressible-ideal-gas-law. The gas specific heat, thermal conductivity and viscosity of the gas mixture are calculated by the mass fraction-weighted-mixing-law, and the species specific heat is obtained by the piecewise polynomial fit of temperature.

In the simulations, the mesh is non-uniformly accumulated at the reaction zone and near the wall surface. In order to determine the optimal mesh density for the solutions, four cases with different number of gird points (2000, 3200, 5000, 8400) are conducted. Figure 2 illustrates the centerline temperature profiles for all the involving cases. The case with 2000 cells, the coarsest case, fails to depict the maximum temperature. However, as the mesh number increases to 5000 cells, the solutions come to a convergence, giving the desired accuracy. Larger mesh number, up to 8400 cells, yields no obvious advantage. Therefore, the case with 5000 cells and a time step of 10^{-5} s is adopted hereafter, considering both the accuracy and the computing time.

3 Results and discussion

3.1 Temperature Distribution

Figure 3 shows that two regions, i.e., combustion region (A) and post-combustion region (B), could be obviously distinguished for all the cases. Almost no preheating zone exists since the high inlet temperature approaches to the ignition

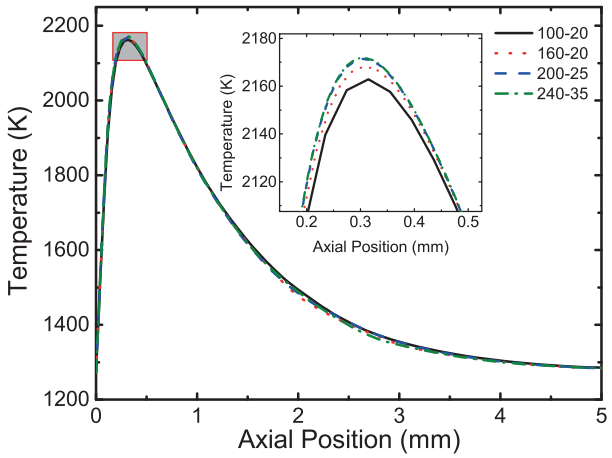

Fig. 2 Centerline temperature profiles for cases with different grid numbers. The inset shows the partial enlarged detail of the temperature profiles around respective maximum. A case is casually selected among all the computed cases for mesh validation,with the parameters $u_0 = 1.4$ m/s, $v_0 = 0$ m/s, $T_{in} = T_s = 1273$ K, $P = 1$ atm, $\Phi = 0.95$.

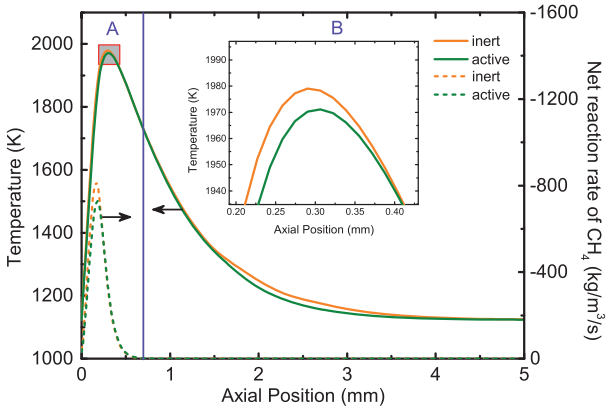

Fig. 3 Centerline temperature profiles for cases with inert or active surface. The inset shows the partial enlarged detail of the temperature profiles around respective maximum. The parameters are $u_0 = 0.6$ m/s, $v_0 = 0$ m/s, $T_{in} = T_s = 1123$ K, $P = 1$ atm, $\Phi = 0.95$. For convenience, hereafter the active and inert surfaces refer to the surfaces with and without surface reactions, respectively.

temperature. Since the isothermal wall is introduced and as hot as inlet gas, no wall thermal conductivity, namely heat recirculation, prevails throughout. Thus the upstream conductive heat flux through the fluid mixture is the only pathway for flammable mixture to warm up to ignite in the very front end of region A. This heat flux is initially conducted from the combustion zone, where the fluid mixture is the hottest. On account of the hottest position locating at the centerline, thus the mixture warming up from the centerline to the wall, ignition occurs and then the flame stabilizes both at centerline instead of the vicinity of the wall, consistent with the case of Ref. 15.

Firstly, we examined the effects of surface reactions on flame temperature, usually defined as the maximum of fluid temperature.[39] It should be noted in Figure 3 that the flame temperature with active surface is approximately 10 K lower than that with inert surface. Moreover, the flame with effects of surface reactions is less stretched especially in region B, and the position of flame temperature slightly moves downstream meaning that the flame propagation velocity slightly decreases. In order to understand above effects of surface reactions on flame structure, the further discussion is conducted as follow.

As shown in Figure 4, flame temperature increases with improving T_{in} and T_s and eventually tends to level off, but is still generally lower than the adiabatic flame temperature. This is because the rate of transverse heat transfer within the fluid is comparable with that of heat release under such small scales, and besides there is no wall upstream thermal conductivity, i.e., the significant approach for preheating mixture.[40–43] However, super-adiabatic flame temperature could be obtained as the inlet velocity exceeds 2.2 m/s (1273 K), which is similar to the results of Ref. 43, but since of more heat release as well as quite hot T_{in} and T_s instead of heat recirculation through the wall. Under the same inlet velocity, higher T_{in} and T_s yield a higher flame temperature for both kinds of surfaces, moreover, with the flame temperature over active surface totally lower than that over inert one. As the inlet velocity increases, the difference between the flame temperatures for both kinds of surfaces tends to diminish and even disappear (at 3.0 m/s), with its maximum emerging at the lowest inlet velocity (0.6 m/s). Interestingly, the flame temperature increases linearly with T_{in} and T_s at the same inlet velocity as shown in Figure 5. It also illustrates that surface reactions have no effects on flame temperature at higher inlet velocity, but the difference could still exists at lower velocities regardless of the inlet and wall temperatures. For methane, its thermal diffusivity is similar to diffusion coefficient since its *Le* (Lewis number) is approximately to unity.[39] Thus to understand these results, *Pe* (Peclet number) could be used to represent the relative significance of radical diffusion to axial convection, defined as Eq. 11. x indicates the axial position from the inlet. *Sc* (0.714), Schmidt number, is taken from Ref. 45 and Re_{in} is evacuated at the combustor inlet.

$$Pe = \frac{\tau_D}{\tau_C} \sim \frac{(H/2)^2/D}{x/u_{in}} = \frac{H}{4x}\frac{\nu}{D}\frac{Hu_{in}}{\nu} = \frac{H}{4x}ScRe_{in} \qquad (11)$$

where τ_C and τ_D represent the time (s) of axial convection and transverse diffusion, respectively. ν is the kinematic viscosity (m^2/s).

The convection time scale of flow to reach the same axial position (x) could be shortened with faster inlet velocity, i.e., higher Re_0, yielding a higher *Pe*. Thus fewer radicals could

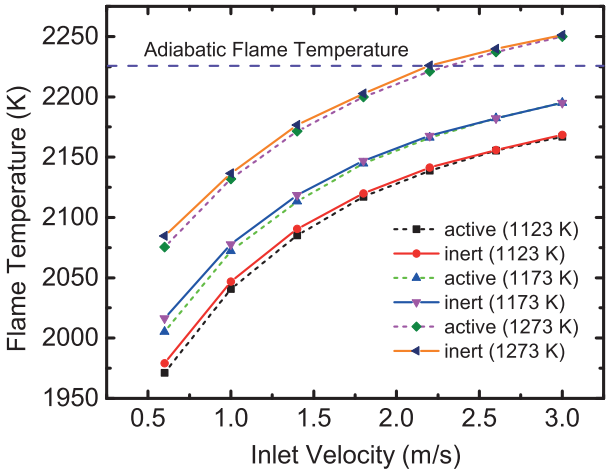

Fig. 4 Effects of inlet velocity on flame temperature for cases with inert or active surface at distinct temperatures (1123, 1173 and 1273 K). Other parameters are $v_0 = 0$ m/s, $P = 1$ atm, $\Phi = 0.95$. The dashed purple line represents the adiabatic flame temperature (~ 2226 K[44]). Note that the blowout or extinction tend to occur, especially for the case with 1123K, when v_0 is above 3.0 m/s or below 0.6 m/s, respectively. Thus we take the intersection of inlet velocities (0.6-3.0 m/s) among the involved cases.

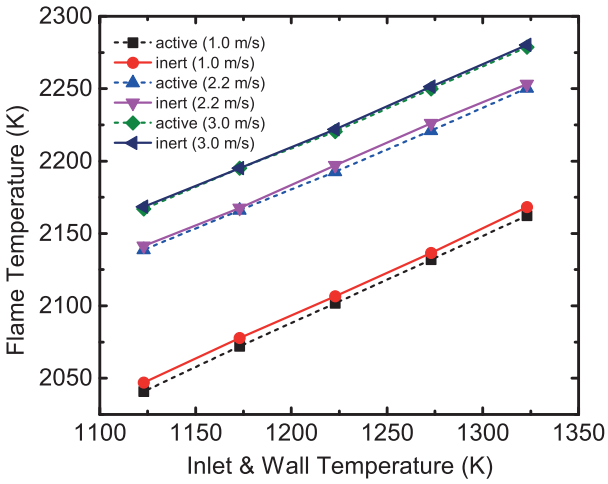

Fig. 5 Effects of T_{in} and T_s on flame temperature for cases with inert or active surface at distinct inlet velocities (1.0, 2.2 and 3.0 m/s). Other parameters are $v_0 = 0$ m/s, $P = 1$ atm, $\Phi = 0.95$.

arrive at the wall surface. Besides, higher u_0 will give higher flame temperature to boost the rates of heat release and radicals generation and then compensate the heat and radical loss towards wall to some extent. So the difference of flame temperatures between both kinds of surfaces tends to diminish at higher *Pe*.

Secondly, we investigated the effects of surface reactions on the post-combustion region. As shown in Figure 6, there are significant axial and transverse temperature gradients in region A, since drastic gas-phase reactions occur, meanwhile releasing heat and then resulting in a sharp rise in fluid temperature. In the post-combustion region B where no drastic reactions occur for the reactants have been almost depleted, the fluid mixture cools down towards the wall temperature. Obviously, there are no significant axial and transverse gradients within region B. The sizes of the two regions vary with operating conditions.

As illustrated in Figure 6 and 7, the size of region A and region B broadens and narrows respectively with increasing u_0 despite with inert or active surface. It is noticeable that a bifurcation appears in centerline temperature profiles for both kinds of surfaces, but could disappear before the exit at low u_0, since reactants could be completely consumed within the reactor. Moderate u_0 has the bifurcation emerge later and keeps it till the exit, meaning incomplete conversion. When u_0 surpasses a critical value, the temperature curves for both kinds of surfaces become entirely identical. Above results could also be explained and divided by *Pe* into three regimes, but x should be replaced by L (length of the reactor): Low and moderate u_0, i.e., low and moderate *Pe*, imply transverse diffusion outperforming or being comparable to axial convection, which causes large quantities of radicals being quenched by active surface and then leave less radicals to react at centerline. Consequently, the centerline temperature with active surface is lower than that with inert surface, in addition, the flame being less stretched by surface reactions. Quite high u_0 (high *Pe*) enhances the axial convection, signifying that quite few radicals diffuse towards the wall surface during the residence, thus the identity could be achieved. Overall, radical quenching should draw particular attention especially at low inlet velocity.

3.2 Radicals Distribution

Actually, the differences in temperature distribution between inert and active surfaces essentially result from the effects of surface reactions on radicals distribution, thus it is necessary to have a further discussion below. Figure 8 demonstrates the simulation results for the mass fraction distributions of H, O, OH and CH_3[31] which are important for flame propagation and stabilization. With the inert surface, the mass fractions of all the radicals, especially H, show a mild transverse gradient, identical with the radical gradients being negligible in microchannels ($R \leq 1$ mm).[15] Therefore, for the sake of simplification, PFR models might be adequate for future investigations on micro-reactor. However, for the active surface, it should be noted that the ratios of the radicals decrease to some extent in the combustion region and large quantities of radicals are adsorbed near the wall surface, showing a significant transverse radical concentration gradient. Thus, obvious radical gradients

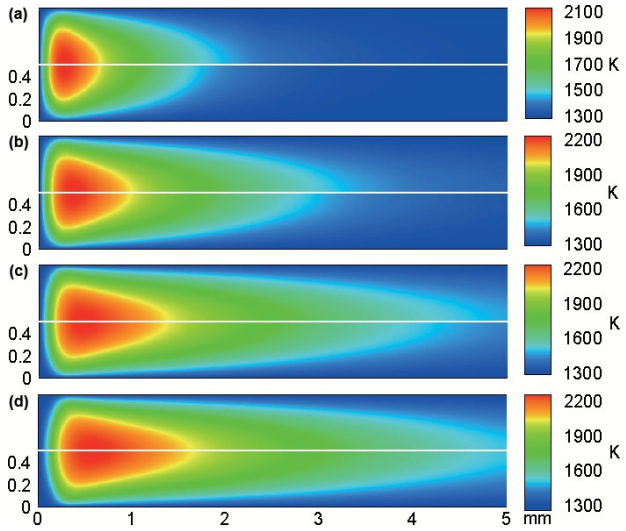

Fig. 6 Temperature contours of micro flame with inert (upper) or active surface (nether) with distinct inlet velocities (u_0 = (a) 1.0, (b) 2.2, (c) 3.4, (d) 4.2 m/s). Other parameters are v_0 = 0 m/s, $T_i = T_s$ = 1273 K, P = 1 atm, Φ = 0.95.

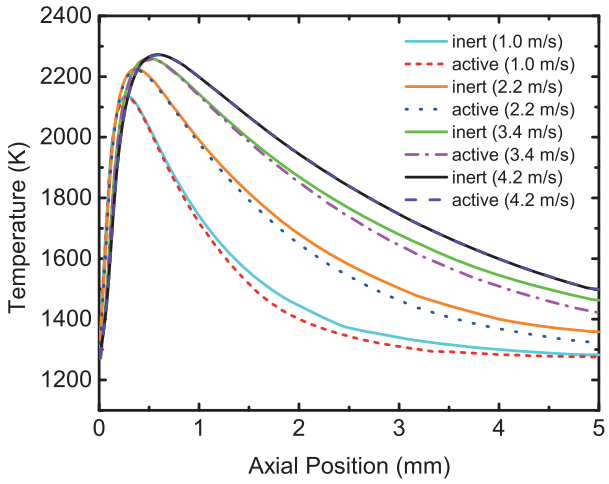

Fig. 7 Centerline temperature profiles for cases with inert or active surface at distinct inlet velocities. The parameters are the same as those in Figure 6.

will still prevail in micro-channels with active surfaces.

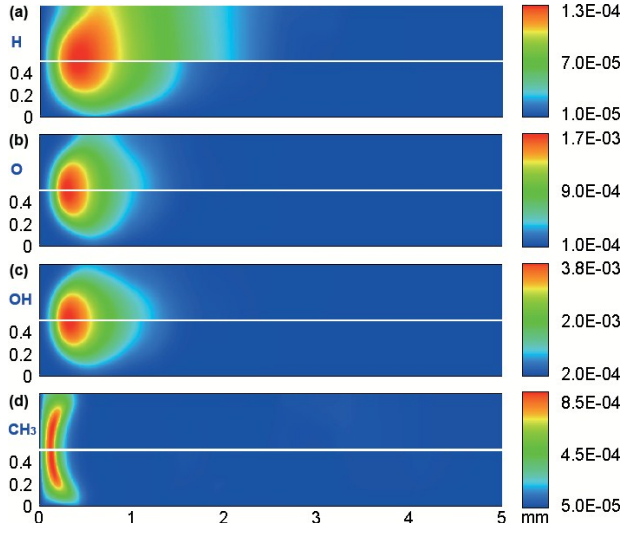

Fig. 8 Mass fraction contours of (a) H, (b) O, (c) OH and (d) CH_3 radicals with inert (upper) or active surface (nether). The parameters are the same as those in Figure 3.

To better understand the effects of surface reactions on flame structure, we focus on the mass fraction distribution near the wall and at the centerline as illustrated in Figure 9. In the combustion region, OH accounts for the most mass fraction among the radicals, followed by O, H and CH_3 in the descending order. They peak almost at the same stream-wise positions except for CH_3. Dehydrogenation of methane is the origin of the chain branching process, thus the mass fraction of CH_3 achieves its maximum earlier in axial direction. Near the wall, in contrast to the radical mass fractions with inert surface, their counterparts with active surface are all significantly reduced (even above 60%) by surface reactions especially in the combustion region. On the contrary, there is no significant difference between the two cases around the centerline in region A, though the radical mass fractions with surface reactions are slightly smaller than their opponents with inert surface. But the difference appears obviously in region B due to the effects of low *Pe* discussed above in Section 3.1.

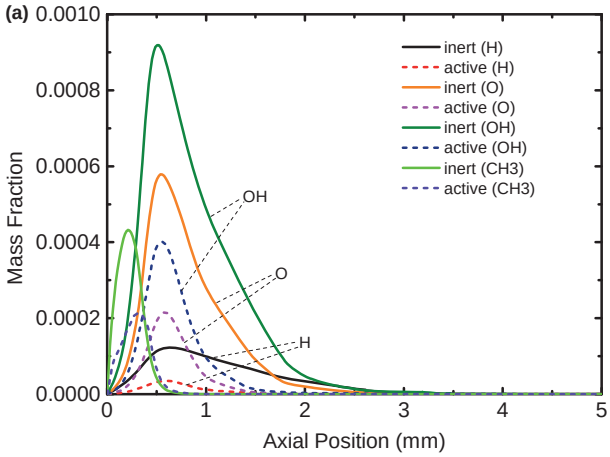

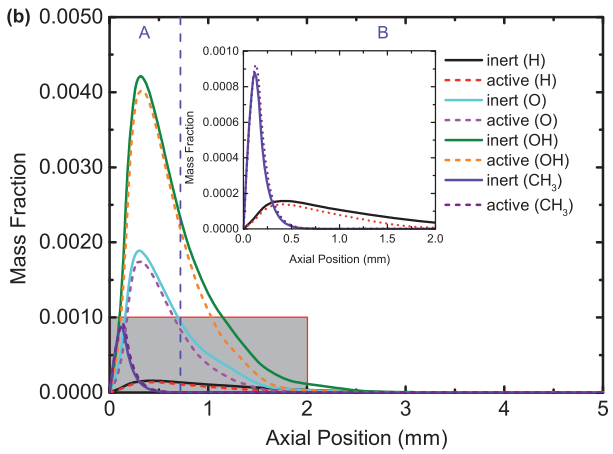

Fig. 9 Mass fraction plots of H, O, OH and CH_3 radicals (a) near the wall and (b) at the centerline. The parameters are the same as those in Figure 3. Note that the mass fraction of CH_3 is not shown in Figure 9(a) for the identification of respective curve. The inset in Figure 9(b) shows the partial enlarged detail of Y_H and Y_{CH_3} distributions. Letters A and B represent the combustion region and post-combustion region, respectively.

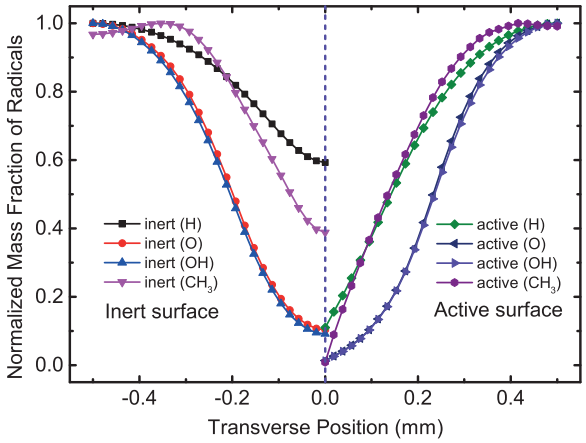

Fig. 10 Wall-normal mass fraction plots of radicals (normalized by respective maximum) in transverse direction. The axial positions are anchored at respective maximum of radical mass fractions. The parameters are the same as those in Figure 3.

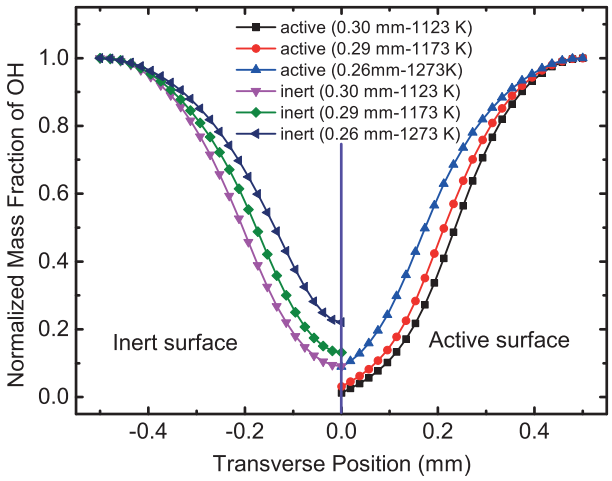

Fig. 11 Wall-normal mass fraction plots of OH radical (normalized by respective maximum) in transverse direction. Note that Y_{OH} peaks at axial positions (0.30, 0.29 and 0.26 mm) for distinct T_{in} and T_s (1123, 1173 and 1273 K, respectively). Other parameters are the same as those in Figure 3.

Figure 10 demonstrates the normalized radical mass fraction $[Y_i]$ distributions in the transverse direction. For both kinds of surfaces, $[Y_H]$ undergoes the mildest decline from the centerline to the wall. This is might due to its higher diffusion coefficient ($1.21 - 3.16 \times 10^{-3}$ m^2/s). $[Y_O]$ and $[Y_{OH}]$ present an identical tendency for both kinds of surfaces since of their similar diffusion coefficients ($3.12 - 8.15 \times 10^{-4}$ m^2/s and $3.07 - 8.01 \times 10^{-4}$ m^2/s, respectively). $[Y_{CH_3}]$ encounters a peak with the inert surface in the transverse direction with a smaller diffusion coefficient ($2.24 - 5.83 \times 10^{-4}$ m^2/s). The mass fraction of each radical (H, O, OH, CH_3) near the surface has a sharper decrease when changing the inert surface to the active surface. In detail, H suffers the largest decay (81.82%), O undergoes the mediate decrease (65.52%), and OH and CH_3 enjoy the smallest reduction (55.56% and 52.38%, respectively). Since we have validated that the radical quenching process is adsorption-limited, the role of each radical adsorption playing in radical quenching could be arranged as Reaction 2, 3, 4, 1 in the descending order. In general, surface reactions affect radical distributions by transverse diffusion and subsequent adsorption, and its effects decrease from the vicinity of the wall to the centerline. One should also infer that surface reactions will give a larger effect to the radical distributions even at the centerline if the channel becomes narrower.

OH radical is chosen as an example to further illustrate the effects of surface reactions on radical distribution since it enjoys the most mass fraction among the four significant radicals. Additionally, it is traditionally considered as the crucial trigger for chain branching and propagation.[44] Figure 11 shows the wall-normal mass fraction profiles of OH radical for both kinds of surfaces at $x = 0.30, 0.29$ and 0.26 mm where respective stream-wise maximum is achieved for distinct T_{in} and T_s (1123, 1173 and 1273 K, respectively). It should be noticed that, as the T_{in} and T_s increase, Y_{OH} peaks earlier in the axial

direction and decreases more mildly for both kinds of surfaces, resulted from the promotion of increasing temperatures towards diffusion coefficient. However, Y_{OH} with active surface still experiences a larger decline in the wall-normal direction than its counterpart with inert surface. Moreover, this difference becomes more obvious especially near the wall as the temperature increases. This is due to that higher temperatures can promote radical adsorption process just as implied by Eq. (8)[29].

4 Conclusions

The effects of surface reactions on the CH_4/air premixed flame within a micro-channel has been numerically investigated with detailed gas-phase and non-catalytic surface reaction mechanisms. The results show that the surface reactions change the flame structure and the conclusions are summarized as follow:

The effects of surface reactions on temperature distribution could be divide into three controlling regimes by the inlet velocity: at low u_0, the flame temperature is reduced and appears downstream and besides the flame structure is less stretched; at moderate u_0, the flame temperature approaches to that with inert surface but the flame shows a obvious contraction in the stream-wise direction especially in the post-combustion region; at high u_0, there is no difference between the temperature distributions for both kinds of surfaces, namely surface radical removing having no inhibition on the temperature distribution any more.

Radicals show great transverse gradients from the centerline to both kinds of surfaces in micro-channels, but suffer sharper declines near the active surface than those near the inert surface due to the radical removing. Furthermore, the difference will become more pronounced especially in the vicinity of the surface as the temperature increases, owing to the promotion of higher temperatures towards diffusion coefficients. Among the radicals, the mass fraction of H, O, and OH & CH_3 near the wall suffers the largest, mediate and the smallest decrease, respectively, when changing the inert surface to the active surface. The adsorption of H should be of the greatest concern. OH and O have the similar distribution profiles for both kinds of surfaces. The inhibition of surface radical removing would be more pronounced within narrower micro-reactors.

Since the effects of surface reactions on flame structure are inclined to be weakened and even negligible as the inlet velocity exceeds a certain level, this would make it feasible to improve the micro-combustion by properly organize the flow field to promote the stream-wise and inhibit the transverse diffusion and conduction.

Acknowledgement

The authors thank the financial supports of National Natural Science Foundation of China with Project No. 51206200, and the Fundamental Research Funds for the Central Universities with Project No. CDJZR12140031.

References

1 R. A. Yetter, V. Yang, M. H. Wu, Y. Wang, D. Milius, I. A. Aksay and F. L. Dryer, *Int. J. Energ. Mater. Chem. Propul.*, 2007, **6**, 393–424.
2 Z. Kaili, S. K. Chou and S. S. Ang, *J. Microelectromech. S.*, 2004, **13**, 165–175.
3 A. P. London, A. A. Ayn, A. H. Epstein, S. M. Spearing, T. Harrison, Y. Peles and J. L. Kerrebrock, *Sens. Actuators, A*, 2001, **92**, 351–357.
4 A. Mehra, X. Zhang, A. A. Ayon, I. A. Waitz, M. A. Schmidt and C. M. Spadaccini, *J. Microelectromech. S.*, 2000, **9**, 517–527.
5 H. T. Aichlmayr, D. B. Kittelson and M. R. Zachariah, *Chem. Eng. Sci.*, 2002, **57**, 4161–4171.
6 H. T. Aichlmayr, D. B. Kittelson and M. R. Zachariah, *Chem. Eng. Sci.*, 2002, **57**, 4173–4186.
7 R. Srinivasan, I. M. Hsing, P. E. Berger, K. F. Jensen, S. L. Firebaugh, M. A. Schmidt, M. P. Harold, J. J. Lerou and J. F. Ryley, *AlChE J.*, 1997, **43**, 3059–3069.
8 I. Ming Hsing, R. Srinivasan, M. P. Harold, K. F. Jensen and M. A. Schmidt, *Chem. Eng. Sci.*, 2000, **55**, 3–13.
9 K. F. Jensen, *Chem. Eng. Sci.*, 2001, **56**, 293–303.
10 D. J. Quiram, I. M. Hsing, A. J. Franz, K. F. Jensen and M. A. Schmidt, *Chem. Eng. Sci.*, 2000, **55**, 3065–3075.
11 Z. Shao, S. M. Haile, J. Ahn, P. D. Ronney, Z. Zhan and S. A. Barnett, *Nature*, 2005, **435**, 795–798.
12 Y. Ju and K. Maruta, *Prog. Energy Combust. Sci.*, 2011, **37**, 669–715.
13 B. Bai, Z. Chen, H. Zhang and S. Chen, *Combust. Flame*, 2013, **160**, 2810–2819.
14 K. T. Kim, D. H. Lee and S. Kwon, *Combust. Flame*, 2006, **146**, 19–28.
15 S. Raimondeau, D. Norton, D. G. Vlachos and R. I. Masel, *P. Combust. Inst.*, 2002, **29**, 901–907.
16 M. Schultze, J. Mantzaras, F. Grygier and R. Bombach, *Proceedings of the Combustion Institute*, 2014, **35**, in press.
17 A. Brambilla, M. Schultze, C. E. Frouzakis, J. Mantzaras, R. Bombach and K. Boulouchos, *Proceedings of the Combustion Institute*, 2014, **35**, in press.
18 G. Pizza, C. E. Frouzakis, J. Mantzaras, A. G. Tomboulides and K. Boulouchos, *Combustion and Flame*, 2008, **155**, 2 – 20.
19 G. Pizza, C. E. Frouzakis, J. Mantzaras, A. G. Tomboulides and K. Boulouchos, *Combustion and Flame*, 2008, **152**, 433 – 450.
20 K. Maruta, K. Takeda, J. Ahn, K. Borer, L. Sitzki, P. D. Ronney and O. Deutschmann, *Proceedings of the Combustion Institute*, 2002, **29**, 957 – 963.
21 O. Deutschmann, *Catalysis Letters*, 2014, in press.
22 H. Karadeniz, C. Karakaya, S. Tischer and O. Deutschmann, *Chemical Engineering Science*, 2013, **104**, 899 – 907.
23 D. G. Vlachos, L. D. Schmidt and R. Aris, *Combust. Flame*, 1993, **95**, 313–335.
24 D. G. Vlachos, *Combust. Flame*, 1995, **103**, 59–75.
25 P. Aghalayam, P. A. Bui and D. G. Vlachos, *Combust.Theory Modell.*, 1998, **2**, 515–530.
26 R. Sotudeh-Gharebagh and J. Chaouki, *Can. J. Chem. Eng.*, 2003, **81**, 1182–1191.
27 C. M. Miesse, R. I. Masel, C. D. Jensen, M. A. Shannon and M. Short, *AlChE J.*, 2004, **50**, 3206–3214.

28 Y. Saiki and Y. Suzuki, *P. Combust. Inst.*, 2013, **34**, 3395–3402.

29 *Chemkin 10112*, Reaction Design: San Diego, 2011.

30 S. G. P., G. D. M., F. M., M. N. W., E. B., G. M., B. C. T., H. R. K., S. S., G. J. W. C., L. V. V. and Q. Z., *GRI-Mech3.0*, 2002, `http://www.me.berkeley.edu/gri_mech/`, (accessed December 2014).

31 D. G. Vlachos, L. D. Schmidt and R. Aris, *AlChE J.*, 1994, **40**, 1005–1017.

32 J. K. Norskov, F. Studt, F. Abild-Pedersen and T. Bligaard, *Fundamental Concepts in Heterogeneous Catalysis*, John Wiley and Sons, Inc, New Jersey, 1st edn, 2014.

33 J. G. Chen, C. A. Menning and M. B. Zellner, *Surface Science Reports*, 2008, **63**, 201 – 254.

34 O. Deutschmann, R. Schmidt, F. Behrendt and J. Warnatz., *Proc. Combust. Inst.*, 1996, **26**, 1747–1754.

35 J. M. Seddon and J. D. Gale, *Thermodynamics and Statistical Mechanics*, The Royal Society of Chemistry, Cambridge, 2001.

36 R. L. Burwell and R. G. Pearson, *The Journal of Physical Chemistry*, 1966, **70**, 300–302.

37 T. Bligaard, J. Norskov, S. Dahl, J. Matthiesen, C. Christensen and J. Sehested, *Journal of Catalysis*, 2004, **224**, 206 – 217.

38 R. J. Kee, F. M. Rupley, J. A. Miller, M. E. Coltrin, J. F. Grcar, E. Meeks, H. K. Moffat, A. E. Lutz, G. DixonLewis, M. D. Smooke, J. Warnatz, G. H. Evans, R. S. Larson, R. E. Mitchell, L. R. Petzold, W. C. Reynolds, M. Caracotsios, W. E. Stewart, P. Glarborg, C. Wang and O. Adigun, *CHEMKIN Collection, Release 3.6*, Reaction Design, Inc., San Diego, CA, 2000.

39 J. Li, S. K. Chou, W. M. Yang and Z. W. Li, *Chem. Eng. J.*, 2009, **150**, 213–222.

40 Y. Ju and C. W. Choi, *Combust. Flame*, 2003, **133**, 483–493.

41 P. D. Ronney, *Combust. Flame*, 2003, **135**, 421–439.

42 T. T. Leach and C. P. Cadou, *P. Combust. Inst.*, 2005, **30**, 2437–2444.

43 D. G. Norton and D. G. Vlachos, *Chem. Eng. Sci.*, 2003, **58**, 4871–4882.

44 S. R. Turns, *An introduction to combustion : concepts and applications*, McGraw-Hill, New York, 3rd edn, 2012.

45 R.-H. Chen, A. Kothawala, M. Chaos and L. P. Chew, *Combust. Flame*, 2005, **141**, 469–472.

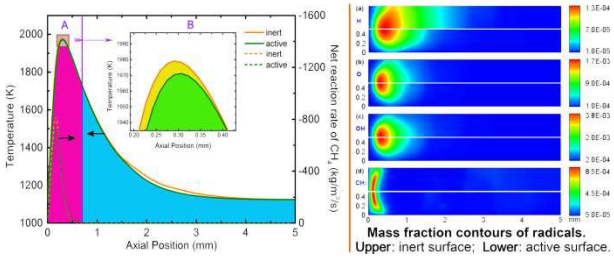

By means of numerical simulation, this paper presents the effects of non-catalytic surface reactions on flame temperature distribution and radicals distribution within a 2D micro planar channel.